Title: Experiments and Modeling of Air-powered Needle-free Liquid Injectors

Author list: Rocco Portaro and Hoi Dick Ng*

Affiliation of authors:

Department of Mechanical and Industrial Engineering, Concordia University, Montreal, Quebec H3G 1M8, Canada

Running title: **Analysis of air-powered needle-free liquid injectors**

*Corresponding author:

Tel.: 1-(514) 848-2424 ext. 3177

Fax: 1-(514) 848-3175

E-mail: hoing@encs.concordia.ca

ABSTRACT

Liquid jet injectors are biomedical devices used for drug delivery without the use of hypodermic needles. These devices generate a high-speed small-diameter liquid jet of sufficient pressure to penetrate the skin and deliver an appropriate amount of medication. In this study, a detailed investigation on needle-free liquid injection systems powered by compressed air is carried out. Experiments are conducted using a custom-built experimental prototype which makes it possible to vary a number of parameters. The experimental results are used to validate a fluid mechanics model for air-powered needle-free injectors. The model, based on the work of Baker and Sanders [*IEEE Trans. Biomed. Eng.*, 46: 235-242, 1999] and Chen et al. [*Drug Deliv. Lett.*, 1: 97-104, 2011], modifies a forcing term that relates the air pressure used to drive the injection to the stagnation pressures of the jet exiting the injector. The results are analyzed to determine which parameters among driver pressure, nozzle diameter, liquid column length, and frictional losses most significantly impact the peak and average stagnation pressures of the jet exiting the air-powered needle-free liquid injector.

Keywords: Needle-free liquid injection, Air-powered system, Stagnation pressure, Fluid mechanics model, Drug delivery, Jet injection

1. Introduction

A needle-free liquid injector is a biomedical device that delivers medication through the creation of a high-speed jet without the use of a hypodermic needle. The development of jet injectors for the administration of medication began in the early 1930's as it was necessary to have a very quick and effective way to immunize the masses against diseases such as polio, influenza, and smallpox [1]. Early jet injectors allowed medical professionals to quickly vaccinate the masses at a rate of up to 1000 immunizations per hour. Liquid jet injectors initially caused many problems, such as pain, bruising, hematomas, incomplete delivery of medication, excessive penetration, and cross contamination [2-5], limiting their widespread use. With advances in the field of drug delivery and micro-fluidics, there is renewed interest in jet injectors, with studies conducted on their mechanism and application to the delivery of existing drug formulations and new drugs, such as DNA-based drugs [6,7].

The mechanics of needle-free liquid jet injection consists of the following general steps: a force generated from a power source is imparted on a cylinder which forces a column of fluid containing the drug through a nozzle, where it exits as a high-speed small-diameter liquid jet of sufficient pressure to penetrate the skin and deliver the appropriate amount of medication. Studies have shown that commercially available injectors produce exit jet velocities greater than 100 m/s and diameters ranging from 100 to 360 μm [7]. The literature shows that commercial injectors can also produce an initial pressure change of 27.5 MPa within 0.5 ms [1,7]. Typical delivery rates for commercially viable injectors range from 0.1 to 1 ml, with a penetration depth of up to 10 mm. At these depths, it is possible to breach subcutaneous layers of the dermis and administer drugs to muscular tissues [8,9]. Jet penetration into skin and the injection quality are determined by a number of jet parameters, such as nozzle diameter, volume to be delivered, jet

stagnation pressure, exit velocity, and stand-off distance (distance between nozzle and skin). A number of recent studies have experimentally shown the dependence of jet penetration into human skin on these parameters, notably by Schramm-Baxter and Mitragotri [10-13]. Besides experimental investigations, analytical models for simulating skin fracture and medicine delivery have been developed [14,15]. There has also been some research into solving the pressure and velocity distribution found within the nozzle by analytical means. Baker and Sanders [16] conducted a continuum analysis whereby they assumed static incompressibility of the fluid, and neglected the effects of viscosity and turbulence. Their model helps characterize the sensitivity of injector design parameters such as piston area, as well as the pressure gradients that will be imposed on the drug to be injected. Recent studies have extended Baker and Sander's model to needle-free injectors powered by springs, the Lorentz force, and piezoelectric actuators [16-19].

This study focuses on the development and analysis of air-powered liquid jet injectors. Although the majority of commercially available injectors are gas/air-powered units [7], no complete model has been developed for simulating the performance characteristics of this particular type of injector. The main goal of this paper is therefore to develop and validate a model capable of predicting the behavior of such devices. The analysis and validation of the developed model are accomplished by constructing a prototype injector that produces jets with geometries and velocities similar to those created by the vast majority of commercially available units. Furthermore, the injector is designed in such a way that the parameters, such as driver pressure, injection chamber length and volume, and nozzle geometry, can be varied. The experimental results are compared to the behavior predicted by the model and analyzed to describe the performance of air-powered needle-free liquid injection systems.

2. Experimental methods

An experimental prototype was designed and built; details of the apparatus were previously reported [20,21]. The prototype injector is designed such that it is representative of the vast majority of commercially available injectors, utilizing a similar power source, propelling the medication in a similar fashion, as well as maintaining consistent jet speeds and diameters. Typical commercially available needle-free injection systems that utilize a gas power source are capable of accelerating a volume of 0.5 ml or less to speeds of up to 200 m/s. Studies show that jet stagnation pressures of 15 MPa are required in order to penetrate the skin [9,14]. The prototype injector was designed based on these standard values. The injector allows a number of parameters, which are fixed on commercially available units, to be varied. The setup is shown in Fig. 1 and the main injector parameters are given in Table 1. Compared to commercial units, a noticeable difference is that the plunger in the prototype is a rigid body. To produce an injection, it is first necessary to set the desired injection volume by adjusting the metering screw, which determines the injection chamber length L. The injection chamber is then filled with the desired liquid and the nozzle is threaded onto the tip, sealing the chamber. The driver chamber can then be pressurized to a desired pressure from an air compressor, which enables repeated charging of the injector. During pressurization, the driver and the injection piston do not move due to the design of the trigger mechanism, which consists of a partially threaded rod that links both the driver and the injection piston. The trigger block locks onto the threads of the metering screw during pressurization, holding the entire injection assembly in place. Once the chamber is fully pressurized and the injection is to be administered, the trigger handle is depressed, thereby disengaging the trigger block from the metering screw, allowing both the driver and the injection piston to move forward and create a high speed jet. The sizing of the design was accomplished by computing the force required to produce the necessary pressure on the area of the plunger as

well as determining the maximum pressure that can be obtained from readily available compressed air. The driver pressure p_D and the jet stagnation pressure p_o can be used to determine the area ratio between the driver A_D and the plunger A_p required to produce a high speed jet capable of penetrating human tissue.

Figure 2a illustrates qualitatively a typical injection administered into 250 bloom ballistics gel, 10 wt% of which was derived from porcine skin (G2500-500G, Sigma-Aldrich, USA) in order to mimic muscle tissue. The penetration was visualized using a blue die mixed with water. As this study focuses only on the fluid dynamics of the injection, jet penetration into the skin is beyond the scope of this paper. The behavior of the jet as it exists the nozzle was recorded using a high-speed video camera (PCO.1200hs). Figure 2b shows images of a jet as it emerges from a 180-μm-diameter nozzle powered at 689 kPa. The jet speed was computed using the interframe time step. The images demonstrate that the jet speed is within the range exhibited by commercially available units. Furthermore, the images clearly show jet divergence. As the jet enters the atmosphere, it fans out and diverges from its initial 180-μm diameter. It is important to note that although the jet diverges dramatically in the atmosphere, it remains confined when penetrating a medium.

The stagnation pressure is the key measurement in this experiment as it can readily be used to validate any fluid mechanics model. It can be used to determine whether the jet emanating from the injector is strong enough to deliver the medication, and hence which depths and type of tissue the injector targets [19]. For quantitative analysis, as described in [19], the stagnation pressure in this experiment was determined using a Honeywell (FSG15N1A) force sensor, which has a range of 0 to 1500 g and a response time of 0.1 ms. Calibration was conducted by imposing known weights and plotting the voltage response of the transducer. Once the force readings were

obtained, it was possible to convert these into stagnation pressures by dividing them by the area of the jet. Since the stand-off distance between the force sensor and the injector nozzle is minimal (~ 1 mm), the jet divergence is assumed to be negligible and thus the area of the fluid jet is equal to the diameter of the high-precision micro-orifice (O'Keefe Controls Co.). The force transducer is also coupled to a signal amplifier, which imposes a gain of 20 on the output voltage, which is read by a Rigol 100 MHz DS1102E digital oscilloscope. The injection process was tracked over the first 5 ms, since within this time the injection provides the peak pressure to penetrate the skin and deposit the medication. To obtain a more accurate portrayal of the injection within these first few moments, the equipment was adjusted to provide the maximum sampling rate within the initial injection period.

The parameters that can be varied to control the stagnation pressure are: driver pressure, nozzle diameter, and injection volume. In this study, the nozzles, with five sizes ranging from 120 to 250 μm (O'Keefe Controls Co.), were manufactured from stainless steel with a precision of 0.00254 mm, which is less than 2% of all orifice diameter sizes. The driver pressure considered in this work ranges from 0.4 to 0.8 MPa and is provided by an air compressor fitted with a precision regulator. Individual nozzle and pressure combinations were tested a minimum of twenty times in order to ensure consistent and reliable results. Furthermore, it was noted that varying the amount of injection volume did not directly influence the stagnation pressure of the jet; rather, it governed the time duration of the injection. As a result, the injection volume was kept constant at 0.1 ml throughout the experiments. The data for these tests were recorded and post-processed for comparisons with the numerical results obtained from the model.

3. Mathematical modeling

By performing a mass balance on the fluid and a force balance on the driving plunger, Baker and Sanders [16] derived a model equation for spring-powered injectors which can predict the stagnation pressure $p(t)$ across the orifice area in terms of the compressibility of the fluid expressed by the bulk modulus, the inertia of the plunger, and mass loss through the orifice:

$$\frac{dp}{dt} = \frac{(B+p)\dfrac{dx_p}{dt}}{L - x_p} - \frac{\dfrac{BA_o}{A_p}\sqrt{\dfrac{2p}{\rho_o}}}{L - x_p} \tag{1}$$

where B is the bulk modulus of the fluid, ρ_o is the initial density, and A_p and A_o are the piston and orifice area, respectively. x_p and dx_p/dt are the position and velocity of the piston that result from the spring release, respectively, and L is the length of the liquid column inside the injector. In Eq. (1), the first term on the right-hand side models the pressurization due to plunger motion and the second term accounts for depressurization due to mass loss.

In order to solve the time-varying behavior of the jet stagnation pressure given in Eq. (1), the initial velocity must be obtained, either by taking measurement data from experiments [17] or by doing a complete force analysis on the injector to develop an equation of motion describing the movement of the driver/plunger assembly [19], which leads to:

$$\frac{d^2 x_p}{dt^2} = \frac{F_D(t)}{m_p} - \frac{A_p\, p(t)}{m_p} - \frac{F_f(t)}{m_p} \tag{2}$$

where F_D and F_f are the driving force and frictional force, respectively. The second term on the right-hand side of this model equation represents the pressure force of the liquid on the piston. Equivalently, it acts as a damping force induced by the pressure differential to dissipate the mechanical work through the hydraulic activity [22]. Since the prototype components of the plunger and the barrel were made from aluminum, no additional compliance is introduced in the model. For the present air-powered injection system, the driving force F_D which moves the

plunger forward is produced by pressurizing the driver chamber. Figure 3a illustrates the geometry and variables within a typical driver chamber of a gas-powered needle-free injection system. The pressure within the chamber can be modeled using the ideal gas law. After the chamber is pressurized to a known pressure, the mass within the chamber can be computed. Once the initial mass of air within the chamber is known, the pressure within the chamber can be computed as a function of driver displacement, i.e.:

$$p_d = \frac{mRT}{V_D(t)} \tag{3}$$

with

$$V_D(t) = (L_o + x_p(t))A_D \tag{4}$$

As the driving force begins to move the piston forward, there is resistance created by both atmospheric pressure acting on the opposite side of the driver face as well as O-ring seals. Figure 3b illustrates a cross section of the opposite side of the driver chamber, which is exposed to the atmosphere through two holes drilled from the front of the injectors.

As the injection is administered, the volume of the secondary chamber is reduced, causing the pressure to increase and thus damping the motion of the plunger as it travels. Subsequently, the secondary chamber is exposed to the atmosphere to prevent pressure build-up as the injection progresses. Therefore, only atmospheric pressure p_a acting on the opposite face of the driver is considered. This force can be assumed to remain constant throughout the injection process and is simply the product of atmospheric pressure and the driver area. This gives:

$$F_D(t) = A_D\left(\frac{mRT}{V_D(t)} - p_a\right) \tag{5}$$

The frictional forces within the mechanism serve to counteract and damp the movement of the driver/piston assembly. The friction is caused by the O-ring seals which make contact and

rub against the inner walls of both the driver chamber and the injection chamber. In order to model the O-ring friction, it must broken down into two components, the first of which consists of the friction force caused by the compression fit of the O-ring into its housing, and the second of which is the result of the thin fluid film generated in the clearance gap between the two components that the O-ring must seal. The forces caused by the compression of the O-ring in the barrel of the injector depend on the force generated by the pressure of the fluid. Consequently, the two major forces causing O-ring friction must be coupled in order to accurately model friction. First, it is necessary to compute the force imposed by the thin fluid layer on the O-ring seal. Here, the approach adopted by Chen et al. [19] is used. This process begins by determining the volumetric flow rate through the small clearance gap between the plunger and the outer barrel of the injector; this flow rate is equivalent to the product of the velocity of the fluid across the gap multiplied by the corresponding cross-sectional area. Consequently, the flow rate can be found by integrating the velocity profile $v(t)$ as a function of an infinitesimal change in gap height, i.e.:

$$\frac{Q(t)}{\pi D} = \int_0^h v(t)dy = \bar{v}(t)h_c = \frac{1}{2}U_p(t)h_c \tag{6}$$

$$h_c = \frac{2Q(t)}{\pi D U_p(t)} \tag{7}$$

where U_p is the moving piston velocity and D is the diameter of the inner wall of the barrel. Hence, the maximum film thickness h_c at the point of zero pressure gradient (i.e., at the point of maximum pressure) can in turn be expressed as a function of volumetric flow rate. For the inertia-free flow of the thin fluid film formed between the moving O-ring seal of the plunger and the stationary wall of the barrel, the simplification of Navier-Stokes equations in association with the continuity equation leads to the Reynolds equation commonly used to analyze the flow of

viscous fluids through small gaps in lubrication problems. Assuming a quasi-steady, incompressible fluid inside the thin film and no gradient in the circumferential direction z or side leakage of the fluid, the one-dimensional Reynolds equation reads:

$$\frac{d}{dx}\left(\frac{h^3}{\mu}\frac{dp_r}{dx}\right) = 6U\frac{dh}{dx} \tag{8}$$

where μ is the fluid viscosity, U is the relative velocity of the sliding boundaries (here $U = U_p(t)$), and p_r is the pressure along the film. Integrating the above equation with $dp_r/dx = 0$ at $h = h_c$ and using Eq. (7), the pressure gradient across the face of the O-ring seal can be expressed as:

$$\left(\frac{dp_r}{dx}\right) = 6\mu U_p\frac{h-h_c}{h^3} = 6\mu U_p\frac{h-\dfrac{2Q(t)}{\pi DU_p(t)}}{h^3} \tag{9}$$

In the case of the injector, if the seal does not leak, there is no flow through the clearance gap $Q(t) = 0$, and therefore:

$$\left(\frac{dp_r}{dx}\right) = \frac{6\mu U_p(t)}{h^2} \tag{10}$$

By integrating the above equation with respect to x, the average of the fluid pressure imposed on the O-ring seal can then be expressed as:

$$\overline{p}_{O-ring} \approx \frac{1}{2}\frac{6\mu U(t)}{h^2}\frac{d}{2} + p(t) \tag{11}$$

where the variable h in this equation can be represented by the film thickness at a wedge-shaped inlet determined by the O-ring and housing dimensions; this dimension is equivalent to the clearance gap of the O-ring. With the pressure imposed by the fluid on the O-ring seal known, the resisting force caused by this pressure is simply the area of the exposed O-ring multiplied by the corresponding pressure, i.e.:

$$F_{fluid} = \overline{p}_{O-ring}\pi Dh \tag{12}$$

The second component of the frictional forces consists of the friction force f_c caused by the compression of the O-ring due to its press fit into the barrel of the injector chamber as well as the compression caused by the pressure exerted by the fluid. In order to determine the force caused by the press fit into the barrel, empirical charts detailing the amount of compression fit as a function of load that an O-ring will produce, as found in [23], can be used. In addition to the force caused by the compression of the O-ring into the barrel of the injector, it is also necessary to take into consideration the transfer of forces caused by the fluid pressure on the O-ring. The fluid pressure that acts on the seal also serves to further increase the compression loading. Studies conducted by Guang and Wang [24] demonstrate that the transfer coefficient between the fluid pressure acting on a seal in relation to the increase of compression force of the O-ring can be estimated to be 1. In other words, the pressure contained within the thin film acting on the seal almost entirely serves to increase the amount of compression forces on the sealing surfaces. Knowing that the coefficient of friction between aluminum and nitrile rubber is 0.2 [19], the resisting force encountered by individual O-ring seals in the injector can be completely described as:

$$f_{O-ring} = 0.2\left(\left(\bar{p}_{O-ring}(t)\right)\pi Db + f_c\right) + \left(\bar{p}_{O-ring}(t)\pi Dh\right) \tag{13}$$

where b corresponds to the contact patch due to O-ring compression measured experimentally; the total frictional forces is $F_f(t) = \sum f_{\text{O-ring}}$.

In summary, solving Eqs. (1) and (2) simultaneously coupled with Eqs. (5) and (13) gives the driver/piston displacement, velocity, as well as jet stagnation pressure. The stagnation pressure can then be further converted to jet speed as it exits the orifice. If it is assumed that viscous losses are negligible across the orifice, then it is possible to use the Bernoulli equation to acquire jet speed from stagnation pressure.

$$V = \sqrt{\frac{2p}{\rho}} \tag{14}$$

4. Results and discussion

To validate the performance of the apparatus and assess the air-powered model, Fig. 4a shows a sample comparison of stagnation pressure variation obtained from the model and experiment, whereby a 200-μm nozzle injects 0.1 ml of fluid driven at 413 kPa. Both results clearly show a pressure peak and the pressure oscillating about a mean injection pressure. As mentioned in previous studies, this peak is important in the formation of a fracture in the skin and the subsequent average delivery pressure determines the depth at which the medication is delivered [25]. The magnitudes of the peak pressure and the average pressure agree with general results reported in the literature [15,19]. Of note, the rise time to peak pressure and subsequent stabilization to the average pressure occur very rapidly. The rise to peak in most of the studied cases occurs within 0.75 ms and the stabilization to the mean pressure is within the same time frame. Figure 4a also depicts a good correlation between the behavior predicted by the model and the corresponding experimental result. Both the peak and the mean pressure for all cases studied are within 15% agreement with the developed model. Furthermore, Fig. 4a illustrates a good match between the oscillation frequencies. Despite the correlation of both experimental and theoretical data, the frequency of the oscillatory behavior about a mean value is variable. A small number of the experiments conducted exhibited more drastic fluctuations in frequency while others did not show oscillation, with stabilization observed immediately after the peak to a mean value. It is also suspected that this behavior is caused by the pressure transducer not sensing small changes as quickly as the injection progresses. Although the transducer has a response time

of 0.1 ms, its sensitivity makes it difficult to acquire both rapid and minute pressure changes. Nevertheless, it is only the average and peak pressures that determine the performance of the injector device as well as the penetration, and thus predicting the oscillatory behavior is of lesser importance. Using Eq. (14), the stagnation pressure also makes the computation of average velocity over the diameter of the orifice possible. Figure 4b shows the velocity profile of the aforementioned case. The peak velocity is in the 150-200 m/s range reported in the literature [1,7,10].

A parametric study of various injector characteristics was performed. The results are summarized in Fig. 5. Figure 5a depicts the peak pressure obtained from nozzles operating at 413, 550, 620, and 690 kPa, respectively. Error bars for the 95% confidence interval are plotted. A visual examination of the data suggests a linear increase in the peak pressure as the driver pressure is increased from 413 to 690 kPa. Using the least-squares linear regression technique, the coefficient of determination, R^2, values were found to exceed 0.80. For the theoretical result, R^2 is higher than 0.96. The R^2 values indicate that the trends of both experimental and theoretical data sets can be well represented by a linear relationship. Furthermore, the experimental data correlate very well to the theoretical model. Obtaining an average value for peak pressure for the different nozzle sizes using the air-powered model made it possible to analyze the experimental data. The maximum variation for the peak pressure is found to be 15% and occurs at lower driver pressures. The greater influence of O-ring friction is a possible explanation for the greater divergence from the theoretical average peak pressure. As O-ring friction is difficult to model because of its variability with pressure, the model seems to over-compensate for this term, causing the theoretical peak at lower pressures to be less than the experimental values. Compounding this error is the sensitivity of the probe. A variation of 2 MPa, as is the case with

the low driver pressure peaks, represents a force variation of 0.0264 N (2.693 g). The transducers range is 0-1500 g. Therefore a difference of 2 MPa would correspond to 0.18% of the transducer's range. These slight differences can thus be attributed to the inaccuracies of the force transducer. Nevertheless, it is possible to conclude that the model is valid in predicting the peak pressures of the injector, given the injector geometry and driver pressure.

The average stagnation pressure after the pressure peak was also analyzed. Figure 5b illustrates the variation of average injection pressure after the pressure peak for various nozzle diameters and driver pressures. The experiment again shows a linear increase in stagnation pressure as the driver pressure increases within the operating range, which agrees with the trend predicted by the air-powered model. The R^2 values from the least-squares regression are 0.8006 and 0.9826, respectively, for the experimental and theoretical correlations. However, the experimental data for average pressure are slightly higher than the predicted values obtained using the air-powered model. The average pressure over the duration of the injection was obtained by finding the mean of the predicted results from the air-powered model at various nozzle sizes and a fixed driver pressure. These values were compared to the experimental data and yielded a maximum variation of ± 2.58 MPa, again occurring when lower driver pressures were utilized. Nevertheless, this variation is acceptable given that the force it represents is only a small fraction of the force transducer's range.

The results shown in Fig. 5 also illustrate that in both theoretical and experimental results, there is no significant deviation between the stagnation pressure values obtained using different nozzle sizes at a given driver pressure. The standard deviations σ of these data sets at increasing driver pressures are: $\sigma_{\text{peak stagnation pressure}}$ = (2.53, 2.09, 2.06, 1.67) MPa and (0.88, 1.13, 0.97, 1.41) MPa and $\sigma_{\text{average stagnation pressure}}$ = (3.86, 1.76, 1.45, 0.63) MPa and (0.16, 0.22, 0.35, 0.42) MPa for

experimental measurements and theoretical results, respectively. The fact that these pressure values with different nozzle sizes are very close to each other (within the experimental error), together with the good statistical regression R^2 values and standard deviations, suggests that the nozzle diameters do not have a large impact on the resulting stagnation pressures. This observation can be explained by analyzing the system in terms of energy. Although the area of the nozzle exit is varied, the area of the plunger remains the same, which means that the total energy imposed on the fluid for a given driver pressure remains the same irrespective of the exit nozzle area. If fluid damping is not present in the system, then one would expect much higher velocities for smaller nozzle areas. However, fluid damping in the system causes there to be more energy dissipation for smaller nozzles due to the coupled hydro-mechanical activity through pressure change and the force required to push the fluid through a smaller exit area. Consequently, the air-powered model predicts roughly the same stagnation pressure for the tested nozzle sizes and an increase of 12 m/s in maximum jet velocity when decreasing from a 250- to 130-μm nozzle diameter. This can be confirmed by analyzing Fig. 6, which compares the stagnation pressures as a function of time, with and without the major contribution of the damping force induced by the pressure change, achieved by removing the second term in Eq. (2) for a constant driver pressure of 413 kPa.

Figure 6a illustrates stagnation pressure with no damping force, clearly showing a significant difference in stagnation pressure between nozzle sizes. A peak of 922 MPa is reached for a 129-μm nozzle in contrast to a peak of 400 MPa for a 259-μm nozzle. An analysis of a chart illustrating stagnation pressure with fluid damping, shown in Fig. 6b, indicates that the pressure peaks for the 129- and 259-μm nozzles are within 2 MPa of each other, representing a jet velocity difference of only 12 m/s. Thus, the decrease in area for smaller nozzles causes an

increase in the energy required to overcome the damping of the fluid as it is forced through the injector orifice. Therefore, the experimental results correlate very well with their theoretical counterparts and for the tested range of nozzle diameters, the variation of nozzle diameter has a very negligible impact on the jet stagnation pressure and velocity.

Another important result is that the pressures obtained for the various experiments are not affected by the stand-off distance. The stand-off distance is defined as the gap between the force transducer and the nozzle exit. Figure 7 illustrates five gap sizes tested with a 180-μm nozzle and a driver pressure of 690 kPa. There is only a variation of 3.5 MPa between the peak stagnation pressures and that of 4 MPa for average stagnation pressures. This variation is due not to the effect of gap distance but rather just the inherent variability of the pressure measurements. This can be confirmed by comparing the traces illustrating the pressure profiles for 5- and 10-mm gaps, respectively. The pressure profile for the smaller gap size exhibits a slightly larger peak pressure by 2.5 MPa, however the larger gap size exhibits a 1.5 MPa increase in average stagnation pressure. If the effect of gap size were substantial, then a larger gap size should dramatically decrease both the average and peak stagnation pressures. However, even with a gap of 25 mm, there is only a very slight decrease in these values. Consequently, the effect of stand-off distance within a practical working distance of up to 25 mm has a negligible impact on both peak and average stagnation values. It is also important to note that when the injector is used to administer medication, the stand-off distance will typically not exist; in other words, the nozzle will be in direct contact with the skin. Nevertheless, due to the limitation of the diagnostics, it was not possible to have the injector contact the force transducer directly in the present experiment, since this resulted in the generation of artifacts in the force readings.

The experimental data also confirmed that the injection chamber volume does not significantly affect the peak or average stagnation pressure. Rather, it affects mostly the period over which the damping occurs. Figure 8 illustrates the model differences in the injection time pressure profile for 25- and 10-mm-long chambers. The model results demonstrate an almost identical match in peak pressure and average stagnation pressure; however, the shorter column oscillates more frequently about the average stagnation pressure than does the longer column. Furthermore, there is also a time shift between the peak stagnation pressures between the column lengths. The longer column requires 0.2 ms more to reach its peak stagnation pressure than does the short column. The time shift can be explained by the fact that the larger volume imparts more damping, thereby shifting the peak of the injection pressure slightly.

The effect of injection volume was also verified throughout these experiments. It was noted that the injection volume affects the duration of an injection. This agrees with the model as it was shown that the chamber length has a negligible effect on both peak and average stagnation pressures, and thus the volume injected can only affect the time period of the injection (see Fig. 9).

In order to further validate that the injection chamber length has a minimal effect on peak and average pressures, a 129-μm nozzle was used in conjunction with a 550 kPa driver pressure, and the injection peak and average stagnation pressures were tracked for various chamber lengths. Figure 10 shows the results. The results for the various chamber lengths are scattered about the predicted model behavior. An analysis of the error bars indicates that there is variation for some of the experimental data points. These variations are more significant for the peak stagnation pressure of longer injection chamber lengths (see Fig. 10a). This can perhaps be attributed to the longer injection chamber column providing more damping at the initial phases of the injection,

consequently resulting in lower peak stagnation pressures. Nevertheless, the values for average stagnation pressure in Fig. 10b agree very well with the model results. When the chamber length was increased from 10 to 40 mm, no specific trend emerged and the test points were scattered near the predicted model behavior, illustrating that the injection chamber length has no effect on average stagnation pressure.

Another important aspect of the theoretical model of the air-powered injectors is the influence of friction. The O-ring friction has an important influence on the magnitudes of the peak and average stagnation pressures as well as the settling time for the oscillatory behavior of the time-pressure profile of a given injection. Figure 11 illustrates the model behavior of friction. Without friction, the model oscillates significantly about an average stagnation pressure, whereas at 50% friction, the model settles to an average stagnation pressure within 2 ms of the start of the injection. Finally, the predicted model behavior with friction settles to an average value within the first 1 ms of the injection and the peak and average stagnation values are 20% lower than those predicted without O-ring friction. It is important to note that varying the effect of O-ring friction experimentally is difficult. This would require manufacturing several piston and driver assemblies and including different amounts of O-ring compression for each assembly. Therefore, it is much more feasible to verify the behavior of the stagnation pressures obtained experimentally and relate these values with behavior predicted by the air-powered model. Consequently, because the behavior of the experimental traces is in good agreement with the model, it is possible to conclude that the model provides a reasonable estimate of mechanical friction throughout the injection process.

5. Conclusion

In this work, the characteristic performance of air-powered needle-free liquid injectors was examined both theoretically and experimentally. The experimental results obtained in this study were used to validate the air-powered model modified based on the work of Baker and Sanders [16] and Chen et al. [19] that predicts the peak and average stagnation pressures of needle-free liquid injectors. The study also verified the importance of several key parameters that influence the performance of an air-powered injector. It was found that the stagnation pressure versus time profile with the new forcing term resembled those obtained in previous studies. There was a clear peak stagnation pressure occurring within 1 ms from the start of the injection followed by a brief oscillatory phase about an average stagnation pressure. The driving pressure was the first parameter to be studied as it validated the developed model and is critical in controlling the jet stagnation pressure. It was determined that as the driver pressure was increased, both the peak and average stagnation pressures increased almost linearly within the operating range considered. It was also shown that varying the injection nozzle diameter did not have any significant impact on the peak or average stagnation pressure. It is expected that smaller-diameter nozzles will produce higher-speed jets and subsequently more stagnation pressure; however, the decrease in diameter causes there to be more fluid damping, and subsequently more energy is dissipated in the fluid for smaller-diameter nozzles. This result demonstrates that for the tested nozzle range, the stagnation pressure for all nozzle sizes at a given driver pressure was approximately equal. It was also observed that chamber length has no significant affect on peak or average stagnation pressure. However, the length of the fluid column did affect the oscillatory behavior about the average stagnation pressure. It was determined that a longer chamber length requires fractionally more time to reach a peak pressure and exhibits a longer period for an individual oscillation compared to those for shorter chamber lengths. The general experimental observations agree

very closely with the developed model. Consequently, the model is valid and can accurately predict the characteristics of the jet emanating from an air-powered needle-free injector.

ACKNOWLEDGMENTS

This work is supported by the Natural Sciences and Engineering Research Council of Canada (NSERC).

REFERENCES

[1] S. Mitragotri, "Current status and future prospects of needle free liquid jet injectors," *Nat. Rev. Drug Discov.*, 5: 543-548, 2006.

[2] R. A. Hingson, H. S. Davis and M. Rosen, "Historical development of jet injection and envisioned uses in mass immunization and mass therapy based upon 2 decades experience," *Mil. Med.*, 128: 516-524, 1963.

[3] R. Worth, J. Anderson, R. Taylor and K. G. Alberti, "Jet injection of insulin: Comparison with conventional injection by syringe and needle," *Br. Med. J.*, 281: 713-714, 1980.

[4] G. Wijsmuller, and D. E. Snider Jr., "Skin testing: A comparison of the jet injector with the mantoux method," *Am. Rev. Respir. Dis.*, 112: 789-798, 1975.

[5] U. Schneider, R. Birnbacher and E. Schober, "Painfulness of needle and jet injection in childern with diabetes mellitus," *Eur. J. Pediatr.*, 153: 409-410, 1994.

[6] M. M. Levine, "Can needle-free administration of vaccines become the norm in global immunization?" *Nat. Med.*, 9: 99-103, 2003.

[7] C. Mohanty, C. D. Mannavathy, D. Srikanth and R. Tabassum, "Needle free drug delivery systems: A review," *Int. J. Pharm. Res. Dev. (IJPRD)*, 3: 7-15, 2011.

[8] S. Mitragotri, "Immunization without needles," *Nat. Rev. Immunol.*, 5: 905-917, 2005.

[9] M. A. Kendall, "Needle free vaccine injection," *Handb. Exp. Pharmacol.*, 197: 193-219, 2010.

[10] J. Schramm-Baxter and S. Mitragotri, "Investigations of needle-free jet injections," *Proc. 26th IEEE Int. Conf. Eng. Med. Biol. Soc.*, 5: 3543-3546, 2004.

[11] J. Schramm-Baxter, J. Katrencik and S. Mitragotri, "Jet injection into polyacrylamide gels: investigation of jet injection mechanics," *J. Biomech.*, 37: 1181-1188, 2004.

[12] J. R. Schramm and S. Mitragotri, "Transdermal drug delivery by jet injectors: Energetics of jet formation and penetration," *Pharm. Res.*, 19: 1673-1679, 2002.

[13] J. Schramm-Baxter and S. Mitragotri, "Needle-free jet injections: dependence of jet penetration and dispersion in the skin on jet power," *J. Control. Release*, 97: 527-535, 2004.

[14] O. A. Shergold, N. A. Fleck and T. S. King, "The penetration of a soft solid by a liquid jet, with application to the administration of a needle-free injection," *J. Biomech.*, 39: 2593-2602, 2006.

[15] K. Chen, H. Zhou, J. Li and G. J. Cheng, "A model on liquid penetration into soft material with application to needle-free jet injection," *ASME J. Biomech. Eng.*, 132: 101005 (1-7), 2010.

[16] A. B. Baker and J. E. Sanders, "Fluid mechanics analysis of a spring-loaded jet injector," *IEEE Trans. Biomed. Eng.*, 46: 235-242, 1999.

[17] J. C. Stachowiak, M. G. von Muhlen, T. H. Li, L. Jalilian, S. H. Parekh and D. A. Fletcher, "Piezoelectric control of needle free transdermal drug delivery," *J. Control. Release*, 124: 88-97, 2007.

[18] R. M. J. Williams, N. C. Hogan, P. M. F. Nielsen, I. W. Hunter and A. J. Taberner, "A computational model of a controllable needle-free jet injector," *Proc. 34th IEEE Int. Conf. Eng. Med. Biol. Soc.*, 2012: 2052-2055, 2012.

[19] K. Chen, H. Zhou, J. Li and G. J. Cheng, "Stagnation pressure in liquid needle-free injection: modeling and experimental validation," *Drug Deliv. Lett.*, 1: 97-104, 2011.

[20] R. Portaro, A. L. Gunter and H. D. Ng, "Analysis of high speed liquid jets emitted from needle free jet injectors," *Bulletin APS 65th Ann. Meeting APS Division of Fluid Dynamics*, 57, F1.56, 2012.

[21] R. Portaro and H. D. Ng, "Experimental analysis of the performance of an air-powered needle-free liquid jet injector," *Proc. 35th IEEE Int. Conf. Eng. Med. Bio. Soc.*, (In press), 2013.

[22] B. Titurus and N. A. J. Lieven, "Model validation and experimentally driven hydraulic damper model refinement," *Proc. 23rd Int. Conf. on Noise & Vibration Eng.*, 1-8: 967-978, 2008.

[23] Darcoid Norcal Seals: "*O-ring Load per Linear Inch of Seal Empirical Chart*," Available: http://www.darcoid.com/images/uploads/pdfs/empiricalcharts

[24] T. H. Guang and D. T. Wang, *Operation Manual of Sealing Components*, Beijing: Mechanical Industry Press, 1994.

[25] A. Arora, I. Hakim, J. Baxter, R. Rathnasingham, R. Srinivasan and S. Mitragotri, "Needle free delivery of macromolecules across the skin by nanolitre-volume pulsed microjets," *Proc. Nat. Acad. Sci.*, 104: 4255-4260, 2007.

FIGURE CAPTIONS

Figure 1. Schematic and photograph of prototype injector.

Figure 2. (a) Penetration of prototype injector into polyacrylamide gel at a driver pressure of 700 kPa and (b) high-speed photograph showing the jet emanating from the injector.

Figure 3. Technical drawing of (a) driver chamber assembly and (b) cross section of venting chamber.

Figure 4. (a) Stagnation pressure and (b) jet velocity as a function of injection time for 200-μm nozzle at 413 kPa.

Figure 5. (a) Peak stagnation pressure and (b) average stagnation pressure as functions of driver pressure.

Figure 6. Stagnation pressure as a function of time (a) without and (b) with fluid damping in the model.

Figure 7. Effect of stand-off distance on stagnation pressure.

Figure 8. Effect of injection chamber length on stagnation pressure obtained using the model.

Figure 9. Effect of injection volume on overall injection time from the experiment.

Figure 10. (a) Peak stagnation pressure and (b) average stagnation pressure as functions of chamber length for a 129-μm nozzle and a 550-kPa driver pressure.

Figure 11. Effect of O-ring friction on stagnation pressure.

TABLE CAPTIONS

Table 1. Prototype injector parameters.

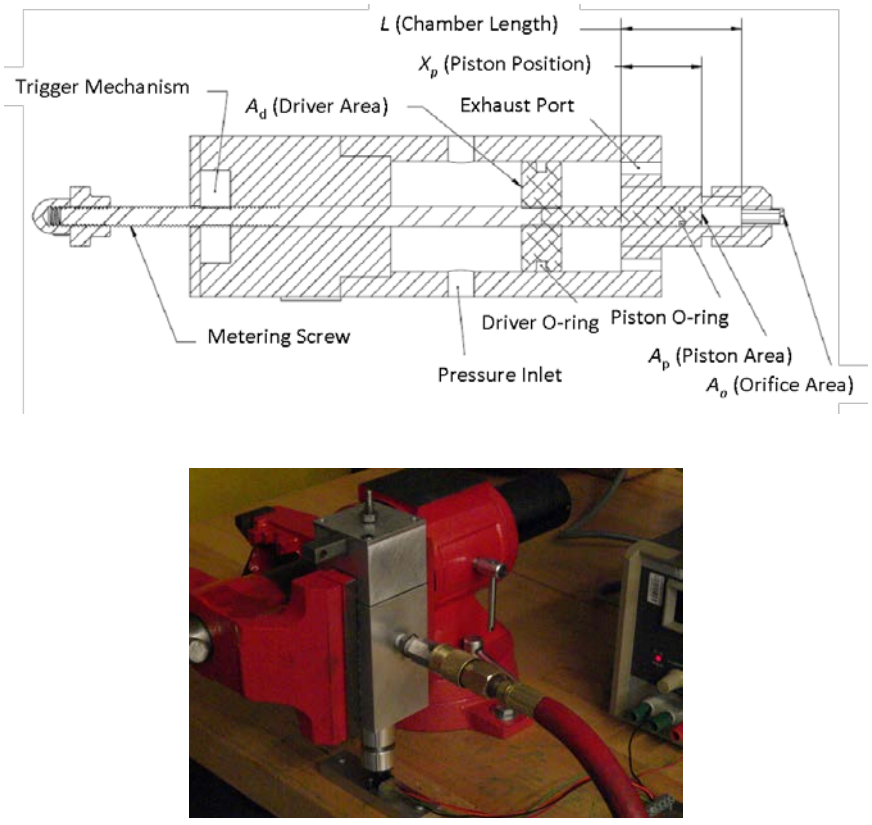
L (Chamber Length)
X_p (Piston Position)
Trigger Mechanism
A_d (Driver Area)
Exhaust Port
Metering Screw
Driver O-ring
Piston O-ring
A_p (Piston Area)
Pressure Inlet
A_o (Orifice Area)

Figure 1.

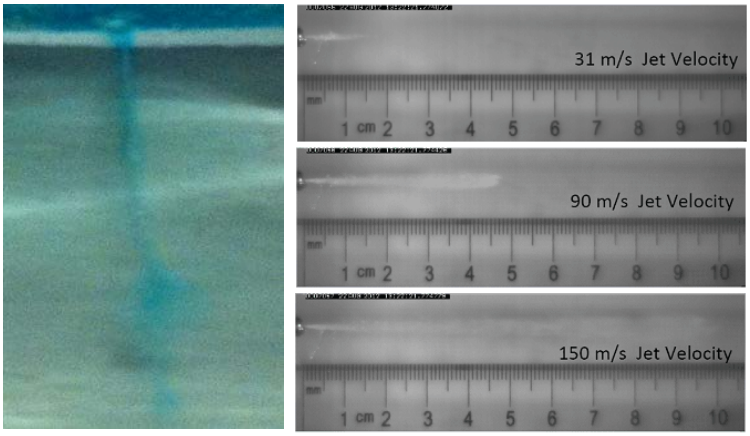
31 m/s Jet Velocity
90 m/s Jet Velocity
150 m/s Jet Velocity
1 cm 2 3 4 5 6 7 8 9 10

(a) **(b)**

Figure 2.

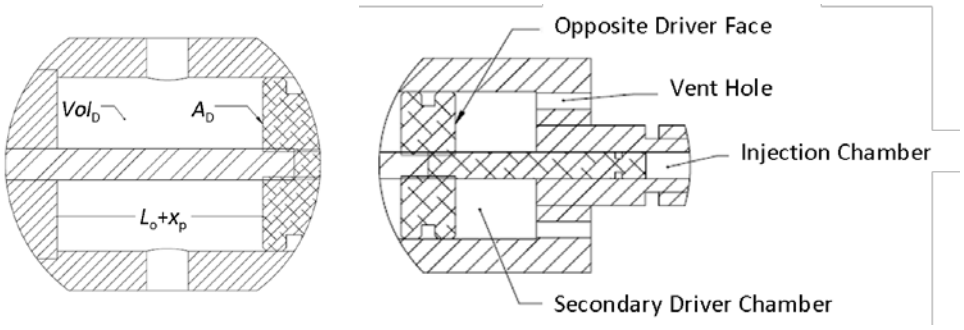
Vol_D
A_D
L_o+x_p
Opposite Driver Face
Vent Hole
Injection Chamber
Secondary Driver Chamber
(a)
(b)

Figure 3.

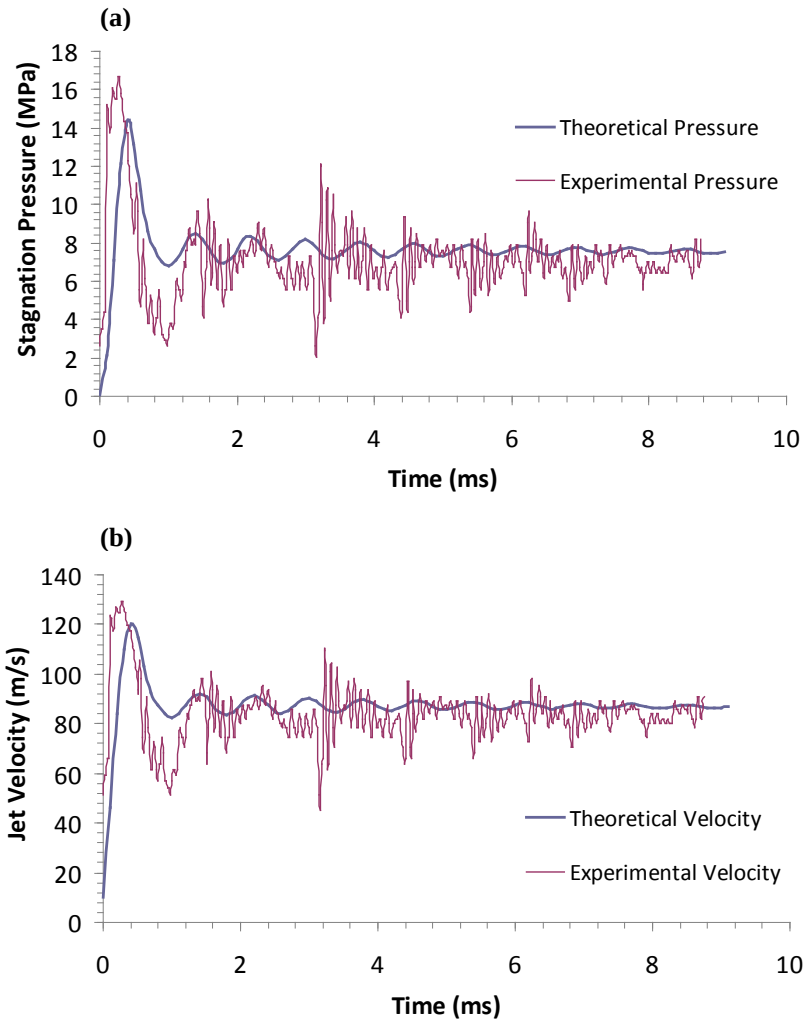
(a)
Stagnation Pressure (MPa)
18
16
14
12
10
8
6
4
2
0
0
2
4
6
8
10
Time (ms)
Theoretical Pressure
Experimental Pressure
(b)
Jet Velocity (m/s)
140
120
100
80
60
40
20
0
0
2
4
6
8
10
Time (ms)
Theoretical Velocity
Experimental Velocity

Figure 4.

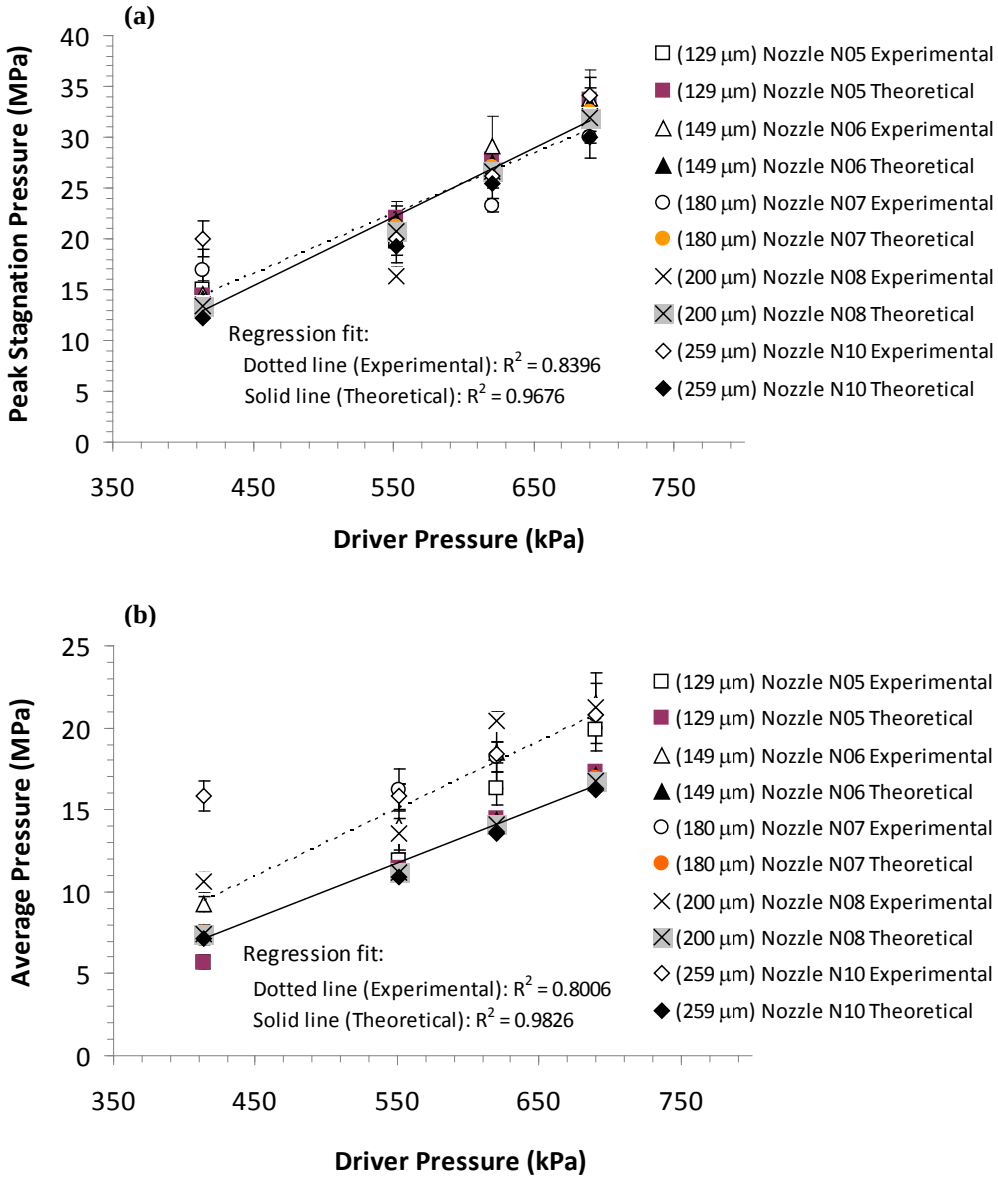
(a)
Peak Stagnation Pressure (MPa)
40
35
30
25
20
15
10
5
0
350
450
550
650
750
Driver Pressure (kPa)
Regression fit:
Dotted line (Experimental): R2 = 0.8396
Solid line (Theoretical): R2 = 0.9676
(129 µm) Nozzle N05 Experimental
(129 µm) Nozzle N05 Theoretical
(149 µm) Nozzle N06 Experimental
(149 µm) Nozzle N06 Theoretical
(180 µm) Nozzle N07 Experimental
(180 µm) Nozzle N07 Theoretical
(200 µm) Nozzle N08 Experimental
(200 µm) Nozzle N08 Theoretical
(259 µm) Nozzle N10 Experimental
(259 µm) Nozzle N10 Theoretical
(b)
Average Pressure (MPa)
25
20
15
10
5
0
350
450
550
650
750
Driver Pressure (kPa)
Regression fit:
Dotted line (Experimental): R2 = 0.8006
Solid line (Theoretical): R2 = 0.9826
(129 µm) Nozzle N05 Experimental
(129 µm) Nozzle N05 Theoretical
(149 µm) Nozzle N06 Experimental
(149 µm) Nozzle N06 Theoretical
(180 µm) Nozzle N07 Experimental
(180 µm) Nozzle N07 Theoretical
(200 µm) Nozzle N08 Experimental
(200 µm) Nozzle N08 Theoretical
(259 µm) Nozzle N10 Experimental
(259 µm) Nozzle N10 Theoretical

Figure 5.

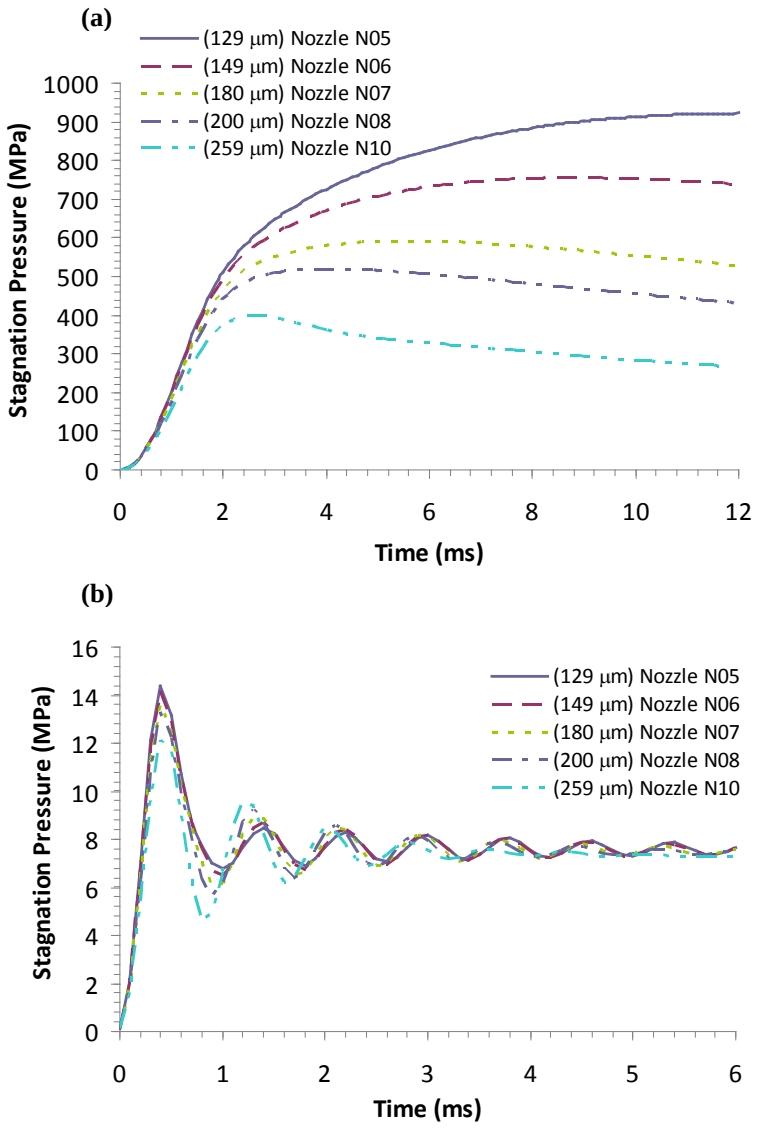
(a)
(129 μm) Nozzle N05
(149 μm) Nozzle N06
(180 μm) Nozzle N07
(200 μm) Nozzle N08
(259 μm) Nozzle N10
Stagnation Pressure (MPa)
Time (ms)
(b)
(129 μm) Nozzle N05
(149 μm) Nozzle N06
(180 μm) Nozzle N07
(200 μm) Nozzle N08
(259 μm) Nozzle N10
Stagnation Pressure (MPa)
Time (ms)

Figure 6.

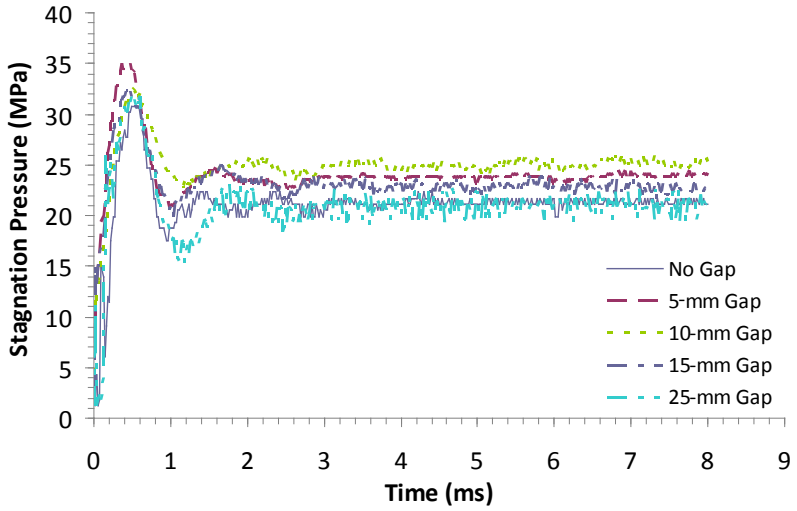
Stagnation Pressure (MPa)
40
35
30
25
20
15
10
5
0
0
1
2
3
4
5
6
7
8
9
Time (ms)
No Gap
5-mm Gap
10-mm Gap
15-mm Gap
25-mm Gap

Figure 7.

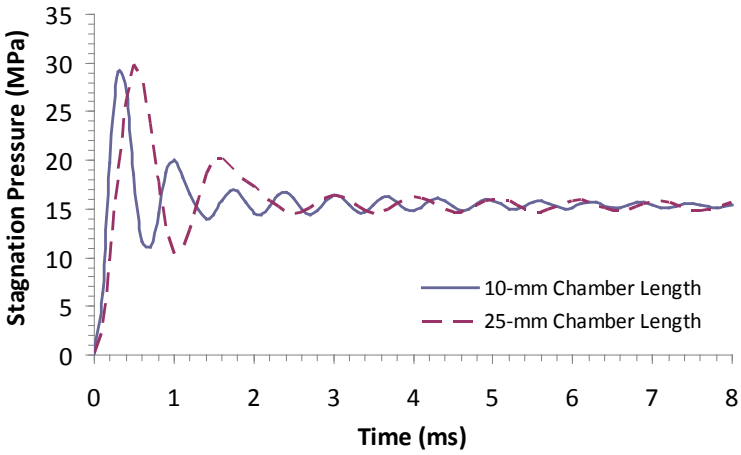
Stagnation Pressure (MPa)
35
30
25
20
15
10
5
0
0
1
2
3
4
5
6
7
8
Time (ms)
10-mm Chamber Length
25-mm Chamber Length

Figure 8.

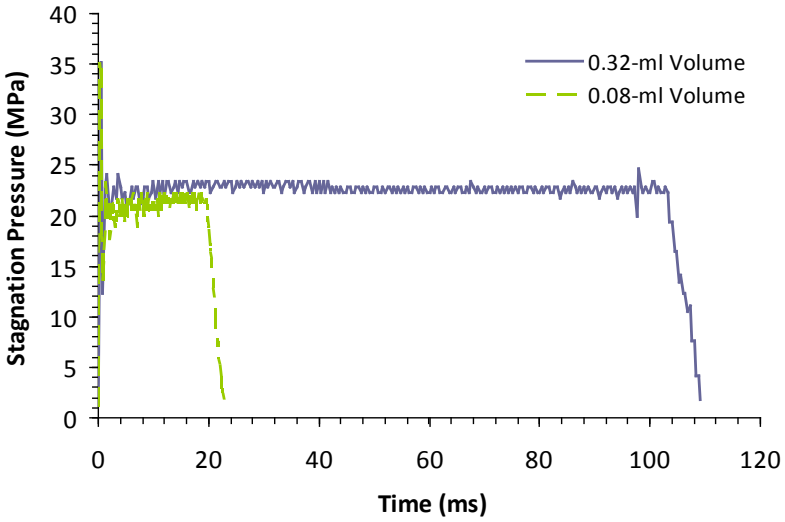
Stagnation Pressure (MPa)
Time (ms)
0.32-ml Volume
0.08-ml Volume
0
5
10
15
20
25
30
35
40
0
20
40
60
80
100
120

Figure 9.

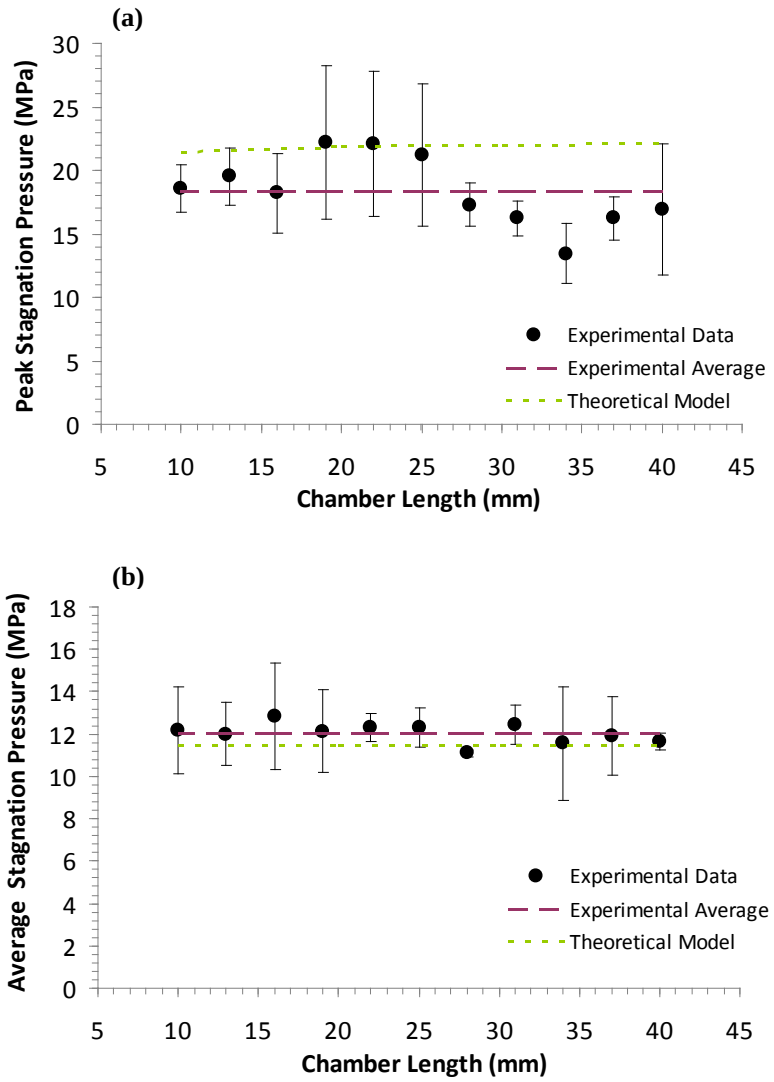
(a)
Peak Stagnation Pressure (MPa)
30
25
20
15
10
5
0
5
10
15
20
25
30
35
40
45
Chamber Length (mm)
Experimental Data
Experimental Average
Theoretical Model
(b)
Average Stagnation Pressure (MPa)
18
16
14
12
10
8
6
4
2
0
5
10
15
20
25
30
35
40
45
Chamber Length (mm)
Experimental Data
Experimental Average
Theoretical Model

Figure 10.

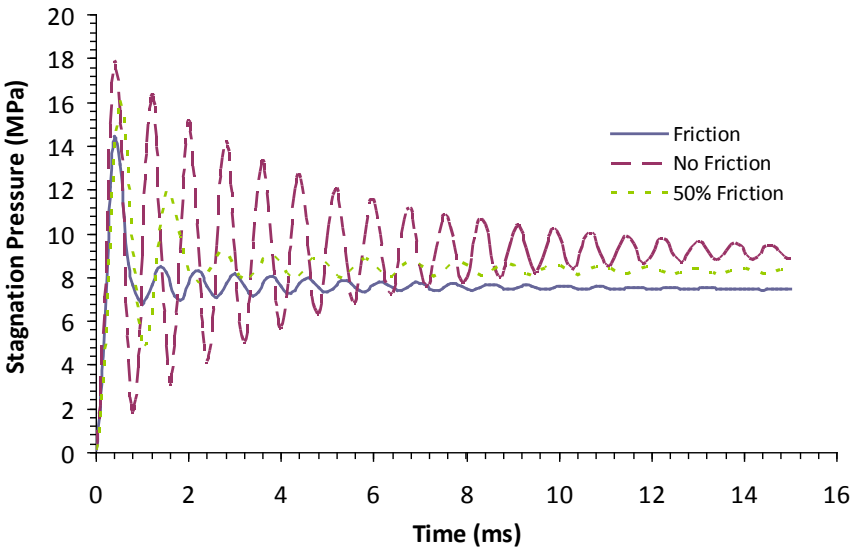
Stagnation Pressure (MPa)
Time (ms)
Friction
No Friction
50% Friction
0
2
4
6
8
10
12
14
16
18
20

Figure 11.

Table 1. Prototype injector parameters.

Injector Parameters	
Nozzle diameter	100 μm - 260 μm
Driver pressure	0.3 MPa - 1 MPa
Injection volume	0 ml - 1.2 ml
Piston diameter	6.35 mm
Driver diameter	38.1 mm
Mass of piston-driver assembly (M_p)	80 g